E3S Web of Conferences **730**, 03013 (2026) https://doi.org/10.1051/e3sconf/202673003013
Soft Soils 2026

Evaluation of Soil Mixing at various depths using Generalized Interpolation Material Point Method

Ying Ma[1*], *Hakimeh* Koochi[1], and *Wojciech* Sołowski[1]

[1] Department of Civil Engineering, Aalto University, Espoo, Finland

Abstract. Deep Soil Mixing has been widely applied in Nordic countries, Japan and other countries to improve the strength and stiffness of in-situ soil. However, the mechanical variability of stabilised soil remains a major issue and quantifying the effects of operational parameters such as blade size, filling level, and rotational speed is difficult because the internal soil flow during mixing cannot be directly observed. This study clarifies depth-dependent deformation mechanisms during mixing through three-dimensional numerical simulations in Uintah using the Generalized Interpolation Material Point method. Calculations reproduce the behaviour of high-water-content kaolin clay with an enhanced, strain-rate dependent, Mohr-Coulomb model. The simulations indicate that soil kinematics are strongly depth-dependent, with peak velocities concentrated near the blade region and rapidly decaying upward and downward, resulting in a limited axial influence zone and persistent mixing heterogeneity. At each depth, the velocity distribution is approximately normally distributed, enabling statistical characterisation of the mixing state and providing a quantitative basis for evaluating operational effects.

1 Introduction

Deep soil mixing is a ground improvement technique that mechanically blends binders such as cement or lime with in-situ soil to form stabilised columns. Since the 1970s, deep soil mixing has been widely used in Japan and Nordic countries, due to its high effectiveness and versatility [1]. It is now applied to a broad range of projects, including improving building foundations [2], embankment support [3], ground reinforcement for shield tunnel construction [4], and artificial island construction [5]. The variety of applications has led to the widespread acceptance and use of the deep soil mixing method in civil engineering, where consistent column quality is essential for design reliability and construction control.

In practice, field-mixed columns usually exhibit lower mean strength and higher variability than laboratory-mixed specimens, mainly because field execution rarely achieves the same degree of homogenisation. Mixing quality is strongly governed by the balance between rotational speed and penetration or withdrawal rates. When the tool penetrates or is withdrawn too quickly relative to its rotational speed, the mixing work delivered per unit length decreases, increasing the likelihood of poorly mixed zones and high binder concentration gradients. Guidance from the Federal Highway Administration (FHWA) links rotation and vertical rates to mixing intensity and recommends monitoring these parameters to improve uniformity [6]. This sensitivity has been reported in field studies, for example, Larsson and coauthors found that installation parameters, especially retrieval rate and the number of mixing blades, significantly affected column uniformity and strength scatter in lime-cement columns [7]. Recent quality control (QC) and quality assurance (QA) reviews similarly identify rotational speed and vertical rates as primary controllable factors for reducing variability [8]. These findings motivate the use of three-dimensional simulations to quantify depth-wise mixing metrics and to optimise operational speeds so that field strength approaches laboratory expectations.

The Material Point Method (MPM) is well suited to large deformation problems [9], and the soil mixing process typically involves such deformations. A developed version of the original MPM, the Generalized Interpolation Material Point Method (GIMP), offers improved precision and numerical stability by modifying the shape functions to account for the finite domain of material points [10]. As a result, cell-crossing errors can be significantly reduced, and the continuity of stress and force fields is improved. These features support the use of GIMP for modelling large deformation behaviour in soft, high-water-content clays during soil mixing.

In addition to large deformations, soil mixing is characterised by intense shearing and rapid remoulding induced by the rotating mixing tool, leading to locally high strain rates. During soil mixing, the rotational and vertical speeds of the blade lead to a high magnitude of strain rates within the soil. This affects the soil behaviour significantly, as the shear strength of clays is strain-rate dependent. Typically, there is an increase of 5–20% for each order of magnitude increase in shear strain rate [11, 12]. Therefore, for soft clays, strain-rate dependency can strongly influence the undrained

* Corresponding author: ying.1.ma@aalto.fi

response under these loading conditions, affecting stress transfer, deformation patterns, and ultimately mixing efficiency. Hence, incorporating strain-rate effects into the constitutive model is essential for representing the mechanical response of soft clays during soil mixing and for improving the predictive capability of numerical simulations.

This study investigates the heterogeneity of deep soil mixing using three-dimensional simulations based on the GIMP method. To quantify mixing, the soil is represented by two coloured constituents, and both mixing index and velocity are evaluated for layers at different depths over time. The results provide insight into depth-dependent mixing efficiency and help identify operating conditions that improve mixing performance and construction efficiency in engineering practice.

2 Numerical setup

2.1 Generalized Interpolation Material Point Method

The simulations were performed using the Generalized Interpolation Material Point Method (GIMP) as introduced by Bardenhagen & Kober [9]. GIMP builds on the Material Point Method (MPM), a particle in cell approach introduced by Sulsky et al. [10] for continuum mechanics problems involving history-dependent materials. However, standard MPM suffers from a cell-crossing instability when dealing with problems involving large displacements [9]. This instability occurs whenever particles cross the boundaries of any cell in the computational background grid and is due to the discontinuity of the grid basis functions used as the interpolation and mapping functions in MPM. These algorithmic errors are reduced in the formulations of GIMP. The GIMP method introduces weighting functions (also known as shape functions or interpolation functions) and gradient weighting functions with a higher degree of smoothness. These functions, which can be interpreted as averages of the basis function and its gradient over the particle domain, are used to map and interpolate data between particles and grid nodes, as well as to calculate internal and external forces. This paper uses GIMP as encoded in the Uintah software (http://uintah.utah.edu) for numerical simulation of the soil mixing process.

2.2 The material constitutive model

In this paper, the undrained behaviour of the fully saturated kaolin clay is represented by an elasto-plastic Tresca model with a non-associated flow rule [13], which has also been used in numerical simulations of fall cone tests for soft clays [14, 15]. The soil mixing process is simulated with a tool rotation rate of 30 rpm. Given the rapid rotational speed and the high-water content (w) considered as 190%, the response is assumed undrained with negligible volumetric change during shearing. Accordingly, the friction angle (ϕ) and dilation angle (ψ) are set to zero.

Table 1. Material and constitutive parameters used in the numerical model.

	Soil	Blade
Type	Kaolin clay	Steel
Density, ρ (kg/m^3)	1552	7800
Shear modulus (kPa)	-	867000
Bulk modulus (kPa)	-	700000
a_1	205	-
b_1	3.86	-
Water content, w (%)	190	-
β	0.091	-
Reference shear strain rate, $\dot{\gamma}_{ref}$ (s^{-1})	0.5	-
Young's modulus ratio (E_u/s_u)	500	-
Sensitivity, S_t	1	-
Remoulding strain parameter, ξ_{95}	1	-
Friction angle, ϕ	0	-
Dilation angle, ψ	0	-
Poisson's ratio, v	0.4999	-

To capture the soil response during mixing, the undrained shear strength (s_u) is described using a combined formulation that accounts for shear strength variation with water content, the effect of shear strain rate ($\dot{\gamma}$) and the effect of strength degradation due to remoulding governed by cumulative plastic shear strain (ξ) [16]. First, the reference undrained shear strength ($s_{u,ref}$) various with water content following an exponential relationship with parameters a_1 and b_1 calibrated for kaolin clay [17].

$$s_{u,ref} = a_1 w^{-b_1} \quad (1)$$

Secondly, strain rate dependency is introduced relative to a reference shear strain rate ($\dot{\gamma}_{ref}$) through a power-law scaling with exponent β [18, 19].

$$s_u = s_{u,ref} \left(\frac{\dot{\gamma}}{\dot{\gamma}_{ref}} \right)^{\beta} \quad (1)$$

Third, strength degradation during continued shearing is captured using an exponential remoulding function governed by sensitivity (S_t) and the remoulding strain parameter ξ_{95}, where ξ_{95} denotes cumulative plastic shear strain required to reach 95% remoulding [16]. Combining these effects, the undrained shear strength is expressed as

$$s_u(\dot{\gamma}, \xi, S_t) = a_1 w^{-b_1} \left(\frac{\dot{\gamma}}{\dot{\gamma}_{ref}} \right)^{\beta} \left[\frac{1}{S_t} + \left(1 - \frac{1}{S_t} \right) e^{\frac{-3\xi}{\xi 95}} \right] \quad (3)$$

In addition, the undrained elastic shear modulus (G_u) is treated as strain rate dependent in the small strain range [20]. To remain consistent with the adopted strain-rate scaling of the undrained shear strength, the undrained elastic shear modulus is expressed using the same strain-rate exponent (β) and the same reference shear strain rate ($\dot{\gamma}_{ref}$)

$$G_u(\dot{\gamma}) = G_{u,ref}\left(\frac{\dot{\gamma}}{\dot{\gamma}_{ref}}\right)^{\beta} \tag{4}$$

The final parameters used are summarised in Table 1.

2.3 Numerical geometry of the model

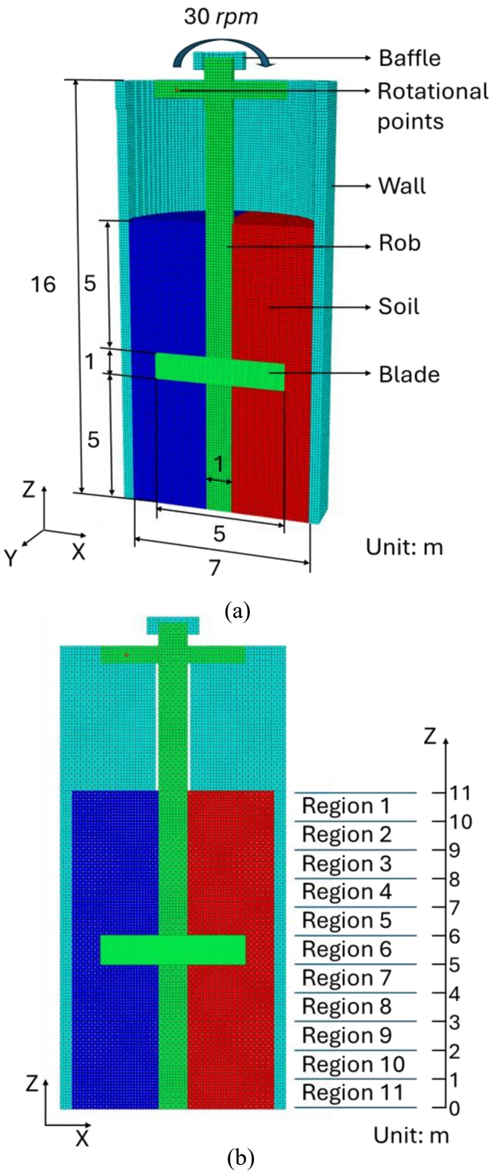

Fig. 1. (a) Cross-section view of 3D numerical model geometry; (b) Soil layers divided along the z-direction.

Fig. 1 (a) illustrates the mixer geometries used in the soil mixing simulation, the framework including a ring-shaped baffle, blade, rotational points, soil domain and mixer wall. To better reproduce the actual mixing process and reduce the potential boundary effects, several additional components were introduced. Specifically, a ring-shaped baffle was incorporated around the top part of the blade to minimise off-axis deviation of the blade during rotation. Two rotational points with prescribed velocity were defined to drive the blade to rotate, representing the mechanical input of the motor. Furthermore, a wall mixer with rigid-like behaviour was implemented to confine the soil domain and simulate the physical boundaries of the mixer to restrict lateral soil movement. The parameters of the numerical model, such as blade size, soil depth and rotational speed, are also shown in Fig. 1. Soil domain is a cylinder with a diameter of 7 m and a height of 11 m. The blade is positioned along the central axis of soil specimen, with the lower edge located 5 m above the bottom of soil domain. The height and diameter of the blade is 1m and 5 m, respectively. The blade rotates at 30 rpm. Fig. 1 (b) shows the soil profile discretised into layers along the Z-axis. A total of 11 layers is defined, with the blade layer located at the mid-depth. This layer division is used to evaluate the non-uniformity of the mixing process.

3 Mixing index

To evaluate the mixing performance quantitatively, the Lacey mixing index M [21] was introduced as an indicator. The approach is based on the statistical theory, where $M = 0$ represents complete segregation and $M = 1$ represents perfect mixing. In this simulation, material particles are labelled as two colours, red (R) and blue (B), to represent two constituents for mixing evaluation. The Lacey mixing index is defined as

$$M = \frac{s_0^2 - s^2}{s_0^2 - s_r^2} \tag{5}$$

where, s_0^2 is the variance of the initial distribution, s^2 is the distribution variance at the current state, and s_r^2 is the variance of the completely mixed distribution. For two colours system:

$$s_0^2 = p(1-p) \tag{6}$$

$$s^2 = \frac{1}{n}\sum_{I=1}^{n}(p_i - p)^2. \tag{7}$$

$$s_r^2 = \frac{p(1-p)}{\overline{N'_R}} \tag{8}$$

where, $\overline{N'_R}$ is the average number of red material particles in all samples. p and p_i denote the proportions of red material particles in the whole domain and in each sample i, respectively:

$$p = \frac{N_R}{N_R + N_B} \tag{9}$$

$$p_i = \frac{N'_R}{N'_R + N'_B} \tag{10}$$

where N_R and N_B are the total numbers of red and blue material particles in the domain, N'_R and N'_B are the corresponding numbers in sample i. The mixing domain is discretised into cubic sampling cells with a side length of 0.5 m. The proportion of red and blue material particles in each cubic sampling cell is evaluated, and the mixing index is calculated every 0.1 s to track the evolution of mixing over time.

3.1 Mixing performance

Previous work investigated the relationship between the mixing index and the radial distance from the blade [22]. In this study, the focus is placed on the vertical influence of blade rotation on the soil with the divided layer shown in Fig. 1 (b). Fig. 2 presents snapshots of horizontal-plane distributions of material-point coordinates at multiple layers along the Z-axis (as indicated in Fig. 1) at t = 9 s. After a period of mixing, the overall mixing state within the cylindrical domain remains highly non-uniform. Soil layers in the vicinity of the blade exhibit relatively homogeneous mixing, whereas the topmost and bottommost layers still contain large contiguous regions of a single colour, indicating insufficient mixing. Overall, the mixing effectiveness decreases with increasing distance from the blade, highlighting the limited axial extent of the blade-induced mixing zone under the present configuration.

In practical deep mixing applications, however, the blade typically undergoes vertical motion involving penetration and withdrawal during operation, which is expected to mitigate such spatial non-uniformity by extending the mixing action to soil layers farther from the blade. The appropriate vertical translation rate requires systematic investigation by examining the temporal evolution of mixing performance. A more detailed time-dependent assessment is provided in the next subsection using the mixing index.

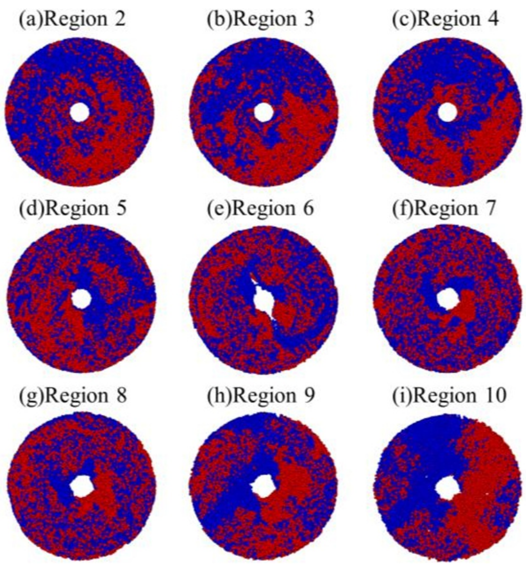

Fig. 2. Mixing performance of different layers at 9s.

To further understand the spatial non-uniformity, the stress response generated by blade–soil interaction was examined. Fig. 3 presents the variation of mean effective stress with depth at different sampling locations at t = 0.1 s. The results indicate that stress concentration around the blade due to the additional local loading on the surrounding soil. It is also observed that sampling points symmetrically with respect to the blade centre exhibit nearly identical stress-depth profiles, indicating an approximately axisymmetric distribution of the stress field in the horizontal plane. Moreover, the simulation was performed without numerical damping, and energy was dissipated exclusively through plastic deformation. This approach improves thermodynamic consistency and enhances the physical realism of the simulation. Numerical stability was maintained by the advanced formulation of the GIMP, which mitigates numerical errors. However, as the adopted Mohr-Coulomb model used is elastic-perfectly plastic, elastic wave propagation is included in the dynamic simulation, leading to fluctuations in the stress field. Furthermore, the soil exhibits behaviour similar to that of a viscous fluid, characterised by non-laminar flow. In general, significant stresses are generated by blade motion, and the material points in the simulation follow complex paths. As the simulation progresses, the overall stress level continues to increase, indicating that blade–soil interaction exerts a sustained influence on the evolution of the stress field.

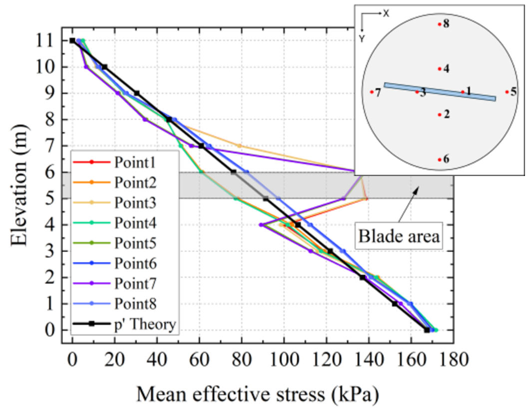

Fig. 3. Variation of the mean effective stress with depth.

3.2 Mixing efficient

The mixing index defined in Eq. (5) is evaluated separately for the regions above and below the blade to quantify the axial extent of blade-induced mixing. The mixing index is computed for each horizontal layer with a thickness of 1 m, and the time history of the mixing index is shown in Fig. 4. The black solid line represents the layer intersecting the blade. This layer exhibits the fastest growth rate of the mixing index over time and attains the largest values, indicating the most effective mixing as shown in Fig. 4.

At the early stage of mixing (0 – 5 s), layers within 2 m above the blade exhibit mixing-index values comparable to those of the blade layer, whereas in the region below the blade, the trend is similar, but lower. However, as stirring proceeds (5 – 9 s), the mixing index in the lower region progressively increases and eventually reaches relatively large values across multiple layers. In contrast, in the upper region, particularly near the free surface, the mixing index remains comparatively small even at later times. This evolving asymmetric axial response may be attributed to the open upper boundary. Although the free surface initially facilitates material rearrangement, it also allows momentum release through surface deformation and radial spreading, limiting sustained accumulation of mixing intensity near the surface. Layers located outside the effective influence range maintain low mixing-index values throughout the process, indicating limited blade mixing and persistent axial heterogeneity.

https://doi.org/10.1051/e3sconf/202673003013

Although the present simulation considers blade rotation at a fixed elevation, the time required to reach a quasi-steady state (approximately 6 s) together with the estimated effective axial influence range (about 2 m and 1 m relative to the upper and lower blade edge) provides a basis for estimating suitable penetration and withdrawal speeds. These estimates offer guidance for subsequent simulations that more closely follow the engineering process by explicitly accounting for blade penetration and withdrawal speed.

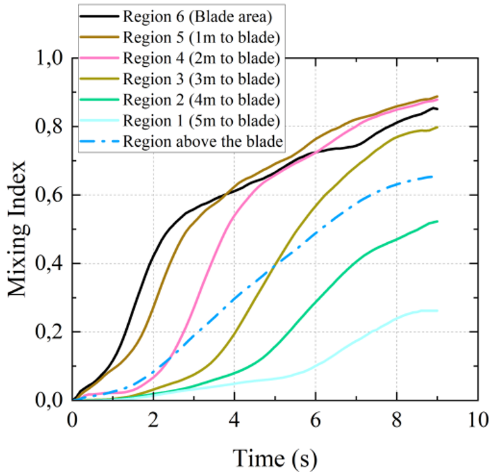

(a)

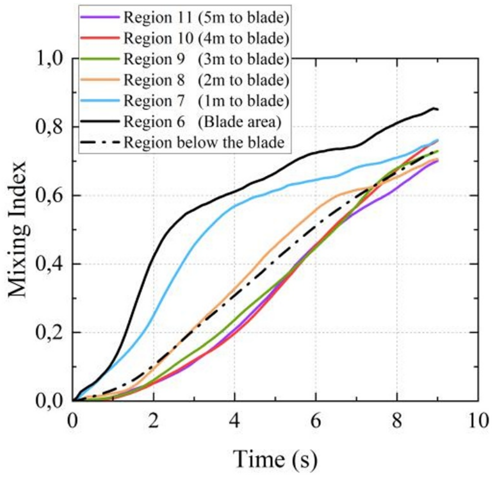

(b)

Fig. 4. Mixing index of different layers, (a) Upper region; (b) Lower region.

3.3 Velocity distribution

During the MPM simulation of the soil mixing process, the point-scale velocity field governs the local shear and mass exchange intensity [24]. Therefore, the evolution of velocity in time and space can be used to explain the heterogeneity of mixing efficiency along with the mixing index. Fig. 5 presents the layer-averaged velocity profiles along the z-direction for different times (0 – 9 s), and the velocity reaches a peak in the blade area and then decays upward and downward, indicating that the stirring action has a limited axial influence range.

In addition, the layer-averaged velocity in all layers increases progressively with time. The layer near the blade accelerates earliest and exhibits the largest increase, and the velocity increment subsequently propagates to the upper and lower layers but rapidly diminishes away from the blade. Moreover, the velocity increment develops faster in the bottom layers, whereas the increment near the surface is relatively slower, demonstrating a clear axial heterogeneous response.

This behaviour can be attributed to the upper region being a free-surface boundary. The momentum input by the blade is more readily released near the free surface through surface deformation, near-surface radial spreading, and energy dissipation in the interfacial region, so the layer-averaged velocity near the surface does not accumulate continuously [24]. In contrast, the lower layers, which are less affected by the free-surface effects, more clearly exhibit a rapid increase in the mean velocity. Consistently, studies on free-surface stirred flows have shown that flow structures and interfacial effects near the free surface can significantly alter the velocity distribution and mixing characteristics. Overall, this velocity profile indicates that the blade-driven motion is transmitted unevenly along the vertical direction, producing a clear axial stratification in the flow field and implying that the effective mixing zone develops differently above and below the blade as stirring proceeds.

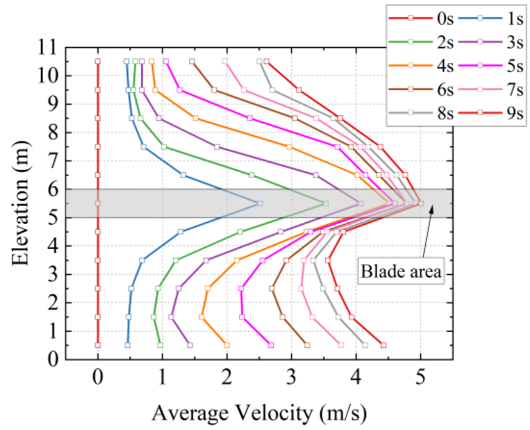

Fig. 5. Layer-averaged velocity profiles along the z-direction for different times.

4 Conclusions

This paper shows simulations of the mixing process based on a 3D Generalized Interpolation Material Point Method, with soft clay approximated by a strain-rate dependent constitutive model.

Although the simulated model does not yet represent a full field-scale configuration, the mixing results indicate high heterogeneity. The main findings of this study are summarised as follows:

1) The mixing process remains non-uniform within the cylindrical domain, with effective homogenisation confined to regions near the blade. Mixing efficiency decreases with axial distance, indicating a limited vertical influence of the blade under the present conditions.
2) The mixing index shows a time-dependent axial asymmetry. Early mixing is confined to about 2 m above and 1 m below the blade, while continued stirring increases mixing mainly

below the blade and leaves the near-surface weakly mixed. These results help inform suitable penetration and withdrawal speeds.

3) The velocity field reveals rapid attenuation of blade-driven motion and a vertically stratified response, which directly governs the axial distribution of the mixing index. Free-surface effects further enhance this heterogeneity in the mixing zone.

The present study is based on a representative-scale configuration with a fixed blade position. Future investigations will focus on engineering-scale models, explicitly account for blade penetration and withdrawal processes, and employ more rigorously validated constitutive models to improve the realism and predictive capability of the simulations.

This research is funded by the Academy Project granted by the Research Council of Finland, decision number 349755.

References

1. M. Kitazume, M. Terashi, The deep mixing method, Vol. 21 (CRC Press, London, 2013).
2. M. Bouassida, A. Porbaha, Ultimate bearing capacity of soft clays reinforced by a group of columns—application to a deep mixing technique, Soils Found. **44**, 91–101 (2004). https://doi.org/10.3208/sandf.44.3_91
3. M. Kitazume, K. Maruyama, Internal stability of group column type deep mixing improved ground under embankment loading, Soils Found. **47**, 437–455 (2007). https://doi.org/10.3208/sandf.47.437
4. Z. F. Hu, Z. Q. Yue, J. Zhou, L. G. Tham, Design and construction of a deep excavation in soft soils adjacent to the Shanghai Metro tunnels, Can. Geotech. J. **40**, 933–948 (2003). https://doi.org/10.1139/t03-041
5. F. H. Lee, Y. Lee, S. H. Chew, K. Y. Yong, Strength and modulus of marine clay-cement mixes, J. Geotech. Geoenviron. Eng. **131**, 178–186 (2005). https://doi.org/10.1061/(ASCE)1090-0241(2005)131:2(178)
6. M. E. C. Bruce, R. R. Berg, J. G. Collin, G. M. Filz, M. Terashi, D. S. Yang, Deep Mixing for Embankment and Foundation Support, FHWA-HRT-13-046 (2013).
7. S. Larsson, M. Dahlström, B. Nilsson, Uniformity of lime-cement columns for deep mixing: a field study, Ground Improv. **9**, 1–15 (2005). https://doi.org/10.1680/grim.9.1.1.58541
8. M. Kitazume, Recent Development and Future Perspectives of Quality Control and Assurance for the Deep Mixing Method, Appl. Sci. **11**, 9155 (2021). https://doi.org/10.3390/app11199155
9. D. Sulsky, Z. Chen, H. L. Schreyer, A particle method for history-dependent materials, Comput. Methods Appl. Mech. Eng. **118**, 179–196 (1994). https://doi.org/10.1016/0045-7825(94)90112-0
10. S. G. Bardenhagen, E. M. Kober, The generalized interpolation material point method, Comput. Model. Eng. Sci. **5**, 477–496 (2004). https://doi.org/10.3970/cmes.2004.005.477
11. A. Casagrande, S. D. Wilson, Effect of rate of loading on the strength of clays and shales at constant water content, Geotechnique **2**, 251–263 (1951). https://doi.org/10.1680/geot.1951.2.3.251
12. J. Graham, J. H. A. Crooks, A. L. Bell, Time effects on the stress-strain behaviour of natural soft clays, Geotechnique **33**, 327–340 (1983). https://doi.org/10.1680/geot.1983.33.3.327
13. Y. Hu, M. F. Randolph, A practical numerical approach for large deformation problems in soil, Int. J. Numer. Anal. Methods Geomech. **22**, 327–350 (1998). https://doi.org/10.1002/(SICI)1096-9853(199805)22:5<327::AID-NAG920>3.0.CO;2-X
14. Q.-A. Tran, W. Sołowski, Generalized Interpolation Material Point Method modelling of large deformation problems including strain-rate effects–Application to penetration and progressive failure problems, Comput. Geotech. **106**, 249–265 (2019). https://doi.org/10.1016/j.compgeo.2018.10.020
15. D. Mohapatra, S. Mohammadi Hasanbarough, M. Saresma, J. Virtasalo, W. T. Sołowski, Numerical simulation of in-situ free fall cone penetrometer tests using the material point method, in UK Association for Computational Mechanics, Durham University, pp. 157–160 (2024). https://doi.org/10.62512/conf.ukacm2024.101
16. I. Einav, M. F. Randolph, Combining upper bound and strain path methods for evaluating penetration resistance, Int. J. Numer. Methods Eng. **63**, 1991–2016 (2005). https://doi.org/10.1002/nme.1350
17. N. Boukpeti, D. J. White, M. F. Randolph, H. E. Low, Strength of fine-grained soils at the solid–fluid transition, Geotechnique **62**, 213–226 (2012). https://doi.org/10.1680/geot.9.P.069
18. G. Biscontin, J. M. Pestana, Influence of peripheral velocity on vane shear strength of an artificial clay, Geotech. Test. J. **24**, 423–429 (2001). https://doi.org/10.1520/GTJ11140J
19. S. W. Jeong, S. Leroueil, J. Locat, Applicability of power law for describing the rheology of soils of different origins and characteristics, Can. Geotech. J. **46**, 1011–1023 (2009). https://doi.org/10.1139/T09-031
20. K. K. Sorensen, B. A. Baudet, B. Simpson, Influence of strain rate and acceleration on the behaviour of reconstituted clays at small strains, Geotechnique **60**, 751–763 (2010). https://doi.org/10.1680/geot.07.D.147
21. P. M. C. Lacey, Developments in the theory of particle mixing, J. Appl. Chem. **4**, 257–268 (1954). https://doi.org/10.1002/jctb.5010040504
22. Y. Ma, H. Koochi, W. T. Sołowski, Simulation of Soil Mixing with Generalized Interpolation Material Point Method, in Proceedings of the IACMAG-2025 conference, Hong Kong, December 18–21 (2025), pp. 820–825. https://doi.org/10.1007/978-981-95-5969-5_116
23. S. S. Hsiau, M. L. Hunt, Shear-induced particle diffusion and longitudinal velocity fluctuations in a granular-flow mixing layer, J. Fluid Mech. **251**, 299–313 (1993). https://doi.org/10.1017/S0022112093003428
24. Q. Li, S. Ma, X. Shen, M. Li, Z. Zou, Effects of impeller rotational speed and immersion depth on flow pattern, mixing and interface characteristics for kanbara reactors using vof-smm simulations, Metals **11**, 1596 (2021). https://doi.org/10.3390/met11101596